Available online at www.sciencedirect.com
SCIENCE DIRECT®
ELSEVIER
Earth and Planetary Science Letters 214 (2003) 203–219
EPSL
www.elsevier.com/locate/epsl

Rare earth and trace element mobility in mid-crustal shear zones: insights from the Mont Blanc Massif (Western Alps)☆

Yann Rolland [a,b,*], Stephen Cox [b], Anne-Marie Boullier [c], Giorgio Pennacchioni [d], Neil Mancktelow [e]

[a] *Labo de Géochronologie/Géosciences Azur, 28 Avenue de Valrose, BP 2135, 06103 Nice, France*
[b] *Geology Department, Australian National University, Canberra, ACT 0200, Australia*
[c] *LGIT, OSUG, BP 53, Université J. Fourier, 38041 Grenoble, France*
[d] *Dipartmento di Geologia, Paleontologia e Geofisica, Via Giotto 1, 35137 Padova, Italy*
[e] *Department Erdwissenschaften, ETH-Zentrum, 8092 Zürich, Switzerland*

Received 13 January 2003; received in revised form 17 June 2003; accepted 2 July 2003

Abstract

The behaviour of rare earth elements (REE) during fluid–rock interaction in mid-crustal shear zones has received little attention, despite their potential for mass balance calculation and isotopic tracing during deformation. In this study, several cases of large REE mobility during Alpine fluid-driven shear zone development in the pre-Alpine granitic basement of the Mont Blanc Massif are considered. On a regional scale, the undeformed granite compositions range within 5 wt% SiO_2 (70.5–75.3 wt%) and magmatic chemical variations are of the order of 10–20%, ascribed to minor effects of crystal fractionation. Major and trace element mobility observed in shear zones largely exceeds these initial variations. Shear zones developed a range of mineral assemblages as a result of shearing at mid-crustal depths (at $\sim$0.5 GPa, 400°C). Five main shear zone assemblages involve muscovite, chlorite, epidote, actinolite and calcite, respectively, as major phases. In most cases, selective enrichments of light or heavy REE (and Y, Ta, Hf) are observed. REE mobility is unrelated to deformation style (cataclastic, mylonitic), the intensity of strain, and to the shear zone's major metamorphic mineral assemblages. Instead, the changes in REE concentrations are ascribed to the alteration of pre-existing magmatic REE-bearing minerals during deformation-related fluid–rock interaction and to the syntectonic precipitation of metamorphic REE-bearing minerals (mainly monazite, bastnäsite, aeschynite and tombarthite). Minor proportions ($<2\%$) of these accessory phases, with grain sizes mostly <20 μm, account for enrichments of up to 5:1 compared to the initial granite whole-rock REE budget. The stability of the REE phases appears to be largely dependent on the altering fluid composition. REE mobility is ascribed to changes in pH and to the availability of CO_3^{2-}, PO_4^{2-}, and SO_4^{2-}ligands in the fluid. Such processes are likely to influence the mobility of REE, Y, Hf and Ta in shear zones.

* Corresponding author. *E-mail address:* yrolland@unice.fr (Y. Rolland).

☆ Supplementary data associated with this article can be found at 10.1016/S0012-821X(03)00372-8

0012-821X/03/$ – see front matter © 2003 Elsevier B.V. All rights reserved.
doi:10.1016/S0012-821X(03)00372-8

1. Introduction

Fluid–rock interaction during shear zone evolution is commonly associated with changes in major element chemistry [1–5]. Changes in major and trace element chemistry are used to infer volume changes, assess mass transfer and investigate aspects of fluid chemistry [1–5]. In general, aluminium, and less frequently titanium and iron, are considered immobile in Alpine shear zones [4,5], but other studies show that almost all elements can be mobilised during mylonitisation [6–9]. Further, experimental investigations have proven that aluminium is unstable in the presence of fluids under greenschist facies metamorphic conditions [10]. Until now, there has been little attempt to use other elements, or trace elements such as rare earth elements (REE), in mass transfer calculations, even though REE, along with Nb–Ta and Zr–Hf, have been widely used as tracers of petrological processes and geodynamic environments. The mobility of REE during hydrothermal fluid–rock interaction has been widely debated in the literature in the past three decades (see [11] for a discussion). It has been demonstrated that REE could be either mobile or immobile depending on specific hydrothermal environments, but the variation in behaviour still remains largely unexplained [12–17]. The mobility of elements during fluid–rock interaction is clearly controlled

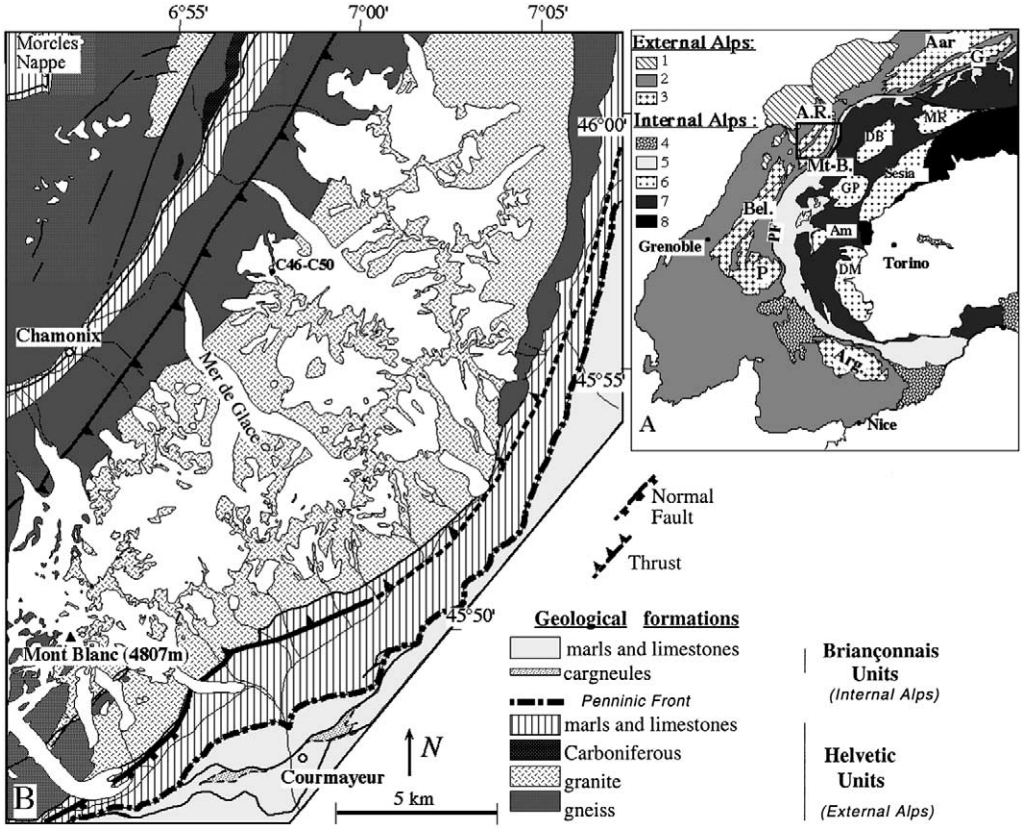

Fig. 1. (A) Geological map of the Alps, with the location of External Crystalline Massifs. 1, Pre-Alpine Nappes (Romand and Swiss Prealps); 2, Dauphinois/Helvetic zone; 3, External Crystalline massifs; 4, Exotic Flysch; 5, Briançonnais Zone; 6, Internal Crystalline Massifs; 7, Schistes Lustrés Complex; 8, Austro-Alpine Units of the western Alps. External Crystalline Massifs: Arg., Argentera; A.R., Aiguilles Rouges; Bel., Belledonne; G, Gotthard; Mt-B., Mont Blanc; P, Pelvoux. Internal Crystalline Massifs: Am, Ambin; DB, Dent-Blanche; GP, Gran Paradiso; MR, Monte Rosa. (B) Simplified geological map of the Mont Blanc massif after [23,24], modified. Location of samples C46–C50 is indicated, and that of other samples is shown in Fig. 3.

by the stability of minerals in which they are incorporated and by the nature of the percolating fluid [3,17–20]. It follows that in order to investigate REE mobility in shear zones, it is necessary to take into account the mineralogical equilibria between fluids and REE-bearing minerals, as well as the role of pH, temperature, redox conditions and of the potential ligands present in the fluid [14,21].

In this paper, we investigate the effects of metamorphic reactions and fluid flow on the stability of elements during shear zone development under greenschist-grade conditions, using the exceptionally well-exposed shear zone network in the Mont Blanc Massif.

2. Geological background

The Mont Blanc Massif is one of several Variscan 'external crystalline massifs' within the western Alps (Fig. 1). It is made of paragneisses, orthogneisses, migmatites and granites [22–25]. The migmatitic gneisses are dated at 453 ± 3 Ma by U–Pb on zircon [26]. The granite intrusion is a Hercynian 35 × 10 km calc–alkaline batholith dated at 300 ± 3 Ma [26]. Several magmatic facies have been recognised, mainly based on the grain size of minerals. From the NW margin to the core of the massif the granite becomes more porphyritic, whereas it is finer-grained near its SE contact [23,24,27]. The intrusive contacts are exposed on both sides, though locally they have been tectonically reactivated during the Tertiary Alpine orogeny. The Mont Blanc Massif is an actively extruding pop-up structure [28,29]. The massif is bounded by a NW-vergent thrust in the NW [30] and by a SE-vergent thrust in the SE [31]. The distribution of faults within the granite has a fan-like arrangement [28,29]. On the SE margin of the Mont Blanc Massif, deformation has been shown to evolve temporally from brittle to ductile in the same shear zones, due to the recrystallisation of phyllosilicates at the expense of feldspars during fluid-assisted deformation (see [32] for a detailed analysis of deformation processes). The timing of shear zone formation is still poorly constrained. In the basement gneiss, some shear zones have been dated at 47 Ma (Ar–Ar on paragonite [33]). In the granite, the shear zones containing biotite–muscovite–chlorite–epidote–quartz–albite assemblages have been dated at 18–36 Ma with the Rb/Sr method [34], but reflect some partial resetting of the granite magmatic age. The Mont Blanc Massif is also well known for its hydrothermal veins, which are formed contemporaneously with the shear zones (e.g. field observations from [35] and references therein). Veins are mainly filled by chlorite, quartz, muscovite, adularia and calcite [36,37]. Vein formation has been dated at 13–18 Ma in the granite using K/Ar and Rb/Sr techniques on adularia and muscovite [38], and at 10 Ma in the basement gneiss (Ar–Ar on adularia [35]).

3. Sampling and analytical techniques

For this study, more than 200 samples have been collected throughout the massif. Fifty shear zone and undeformed granite samples were selected for petrographic study (see Section 4). Out of these samples, five samples of undeformed/unaltered granite (see Section 5), and 31 samples of deformed/altered granite, largely from mylonitic shear zones, were selected for geochemical analysis.

Whole-rock major, trace and REE were analysed at Geoscience Australia (GA) in Canberra. Major and trace element analyses were performed by X-ray fluorescence spectrometry using a Philips PW2404 4 kW sequential spectrometer with a Rh tube. REE were analysed by solution inductively coupled mass spectrometry (ICP-MS).

Mineral compositions were determined by electron probe microanalysis (EPMA). The analyses were carried out at 15 kV and 1 nA using a JEOL 6400 scanning electron microscope (SEM) equipped with an Oxford Instruments light EDS detector and Link ISIS SEMquant software, at the ANU Electron Microscopy Unit. Natural samples were used as standards. Backscattered electron (BSE) imaging was used to locate and identify REE minerals.

Samples with selected REE minerals of size > 50 μm were analysed by laser-ablation ICP-

MS (LA-ICP-MS) at the Research School of Earth Sciences (ANU, Canberra). Samples were ablated with a pulsed 193 μm ArF LambdaPhysik LPX 1201 UV Excimer laser with constant 90 mJ energy, a repetition rate of 5 Hz and a pit diameter of 32 μm. Before ablation, background counts were collected for 30 s, and acquisition time was fixed at 30 s. Power density at target was about 0.25 GW (7 J/cm^{-2}). A mixed Ar–He (with minor H_2) carrier gas transported the ablated material from the sample cell into a flow homogeniser and to an Agilent 7500 ICP-MS. The carrier gas setting was ~1.15 l/min with 0.3 l/min He. Plasma power was 1250 W. Masses were measured in peak jumping mode, 1 point per peak and 0.015 s per mass. Additional information about LA-ICP-MS measurements can be found in [39].

4. Shear zone description and metamorphic conditions

The shear zone network of the Mont Blanc Massif has two main components, one trending 060° with a dextral strike-slip sense and the other N–S with a sinistral sense. Shear sense is deduced from stepped striae and slickenfibres and from microscopic analysis of sigma and delta porphyroclasts. Deformation is always transpressive and related to a lineation with an average plunge of 66° (average of 362 values). The 060° dextral component and the N–S sinistral component of shear zones are consistent with an overall horizontal NW–SE shortening and vertical extension at the scale of the massif. Mylonites and cataclasites occur in both sinistral and dextral shear zones. Cataclasites are mainly found in the first 2 km of the massif's SE rim and locally at the NW side of the massif. They are formed mainly at the onset of shear zone development. The evolution from cataclasites to mylonites is observed in both space and time within individual shear zones, with features demonstrating a progressive transition from brittle to subsequent ductile deformation during reaction weakening associated with the transformation of feldspars into phyllosilicates [32].

The mineral assemblages produced during cataclasis and mylonitisation consist dominantly of albite, muscovite, green biotite, epidote, chlorite, and titanite. The occurrence of muscovite+biotite assemblages implies minimum temperatures of ca 400°C [40], in agreement with the fluid inclusion studies on vein quartz (temperatures of 350–400°C at pressures of 0.25–0.3 GPa [36,37]). Muscovite is stable together with K–feldspar, biotite, albite and quartz, which is the appropriate assemblage for the use of the phengitic barometer of [41]. The muscovite compositions obtained by microprobe analysis have homogeneous Si contents of 3.37 ± 0.08 per formula unit (2σ), based on 84 measurements from samples throughout the massif. These values indicate pressures of 0.8–1 GPa at temperatures of 410 ± 10°C, using the phengitic barometer of [41]. The discrepancy of fluid inclusions and phengitic barometer results has led us to use a third method, based on thermodynamic equilibria between phyllosilicates in a muscovite–biotite ± chlorite ± epidote-bearing sample (see [42] for the approach and methods, using the data from [43,44]). Calculations of pressure and temperature, based on the intersection of independent mineral equilibria, provide estimates of 0.5 ± 0.05 GPa and 400 ± 25°C (2σ; Fig. 2). Similar estimates, within error, were obtained from other shear zone samples, providing evidence

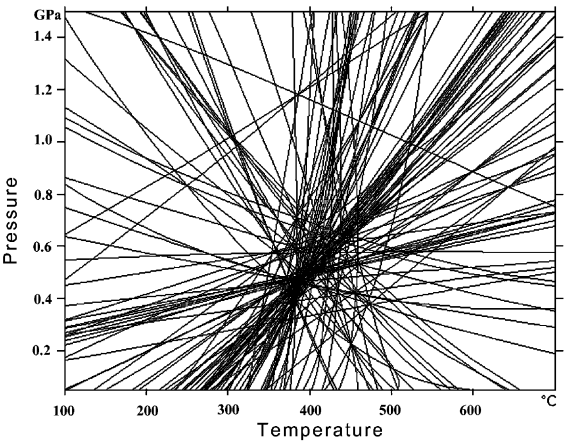

Fig. 2. Typical pressure–temperature diagram obtained for a muscovite–biotite ± chlorite ± epidote shear zone sample. Lines drawn in the figure are the independent equilibria computed from EPMA values following the approach of [42] using the data of [43,44].

that the conditions of formation of the shear zones are those of the upper greenschist facies at mid-crustal depths.

5. Geochemistry of the Mont Blanc granite

To establish the range of initial magmatic chemical heterogeneity within the undeformed granite prior to the development of shear zones, we have compiled the data available from the works of Marro and Bussy [24,27]. A synthesis of the major element data obtained by these authors is displayed in Table 1[1], based on 46 analyses of the porphyritic central facies and on 10 analyses of the fine-grained marginal facies. This synthesis shows that the fine-grained marginal facies is slightly more silica-rich (SiO_2 up to 75.3 wt%) and more depleted in other oxides than the porphyritic core (SiO_2 down to 70.5 wt%), as a result of magmatic fractional crystallisation (see [24] for a complete analysis of magmatic processes). In this study, we have analysed a further five samples of porphyritic and fine-grained facies from across the Mont Blanc granite. Major element analyses of these five samples are within the 2σ compositional range of the Bussy and Marro analyses (Table 2[1]). The variability of REE in the undeformed granite was investigated via a comparison of these five samples with partial REE analyses of eight granite samples from [24]. As indicated in Table 2[1], these two data sets show similar REE contents (at ±12–20%, 2σ average). In conclusion, the initial heterogeneity of magmatic compositions of the granite protolith range within 12–20% and can be explained by minor amounts of crystal fractionation. As we will see in the next section, these initial magmatic variations are far below those ascribed to fluid–rock interaction and volume change in the shear zones.

6. Geochemistry of shear zones

Three main mineral assemblages can be distinguished in the shear zones, which correspond to three domains in the Mont Blanc Massif (Fig. 3): (1) the northwestern domain of mainly epidote-bearing assemblages (e.g. C7), (2) the central domain of mainly chlorite-bearing assemblages (e.g. C33), and (3) the southeastern domain of mainly muscovite ± biotite ± titanite-bearing assemblages (e.g. MB64). Within this third domain, localised actinolite-bearing mylonites (e.g. MB61) and calcite-bearing shear zones (e.g. MB107) are also present. The type of assemblage is not a function of the style or amount of deformation, as these three main mineral associations were found in cataclasites, mylonites and ultramylonites. Rather, the variations in alteration assemblages are interpreted to reflect variations in fluid chemistry and styles of fluid–rock reaction across the Mont Blanc Massif.

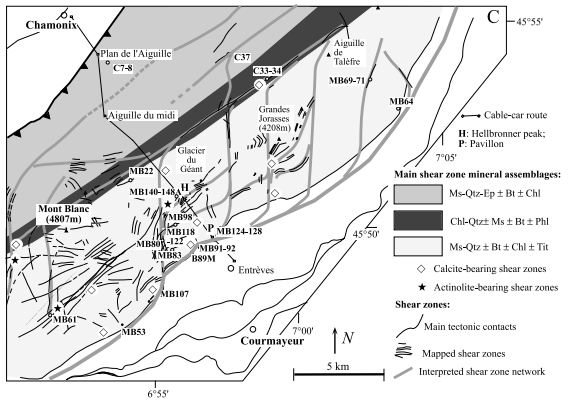

Fig. 3. Structural and metamorphic sketch map of the Mont Blanc Massif. The location of samples selected for geochemical analysis is also shown. Bt, biotite; Chl, chlorite; Ep, epidote; Ms, muscovite; Phl, phlogopite; Qtz, quartz; Tit, titanite.

6.1. Major element geochemistry

In Fig. 4 and Table 3[1], we compare the major element concentrations of representative Mont Blanc Massif shear zones with those of the undeformed Mont Blanc granite (compositional range expressed by 2σ bars). The bulk-rock composition of the various shear zones shows a much greater range than the variation in the initial magmatic composition. The behaviour of major elements is partly due to the effect of quartz dissolution (or

[1] See online version of this article.

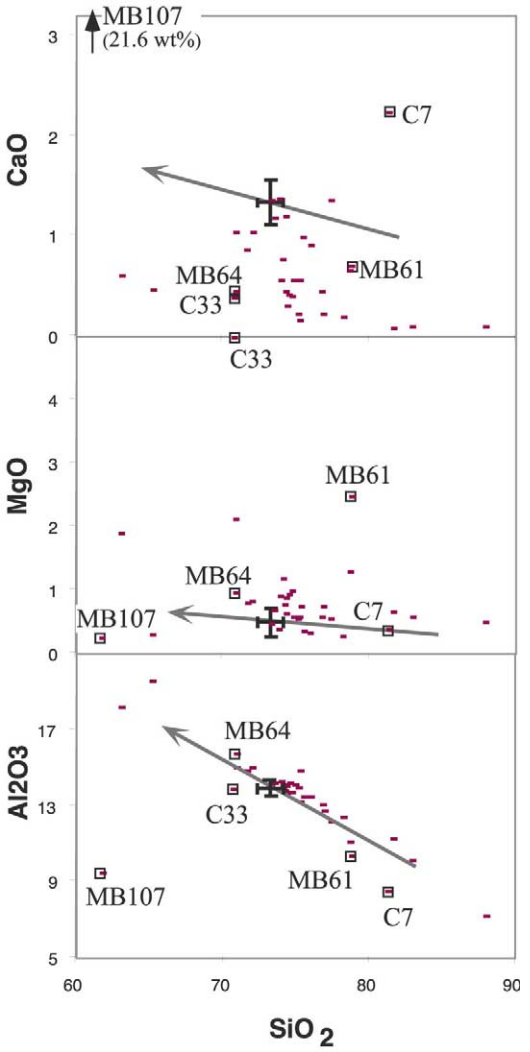

Fig. 4. Harker diagrams representing the major oxides' composition versus SiO_2 for all the analysed Mont Blanc shear zones. Shear zones chosen as representative of a given metamorphic assemblage are labelled, and indicated by squares. Concentrations (in wt%) are normalised to 100%. The initial composition of the Mont Blanc granite is shown by the cross (2σ bars represent the compositional variation in the granite). Model silica enrichment or depletion trends are shown as arrows, based on a mass balance calculation of silica subtraction (or inversely, addition) from the average undeformed granite composition.

inversely, precipitation (indicated by the arrows in Fig. 4). However, except in the Al_2O_3 diagram, elemental variations between shear zones greatly exceed the effects that could be ascribed to silica variation. Al_2O_3 variations fit the modelled variations of concentrations due to quartz precipitation/dissolution (arrow in Fig. 4), showing that Al remained relatively immobile. Only sample MB107 is remarkably outlying the trend, but this can be explained by precipitation of calcite (see below).

With respect to average granite values, the behaviour of major elements is clearly related to the main mineral assemblage type described above in shear zones from three areas in the massif (Fig. 4). *Epidote*-bearing shear zones (e.g. sample C7), have very high CaO and Fe_2O_3, but low K_2O and Al_2O_3 contents (Table 3[1]). *Chlorite*-bearing shear zones (e.g. sample C33), are enriched in Fe_2O_3 and MgO and depleted in Na_2O, K_2O and CaO. *Muscovite* ± titanite-bearing shear zones (e.g. sample MB64) are depleted in SiO_2 and consequent oxide enrichments are likely due to a volume-loss effect (as will be discussed in Section 6.3). *Actinolite*-bearing shear zones (e.g. sample MB61) have high Fe_2O_3, MgO and CaO, and low K_2O contents relative to other shear zones. Finally, *calcite*-bearing shear zones (e.g. sample MB107), bear strong enrichments in CaO and correlated depletions in all other oxides.

In the following section, we examine if the behaviour of REE is also correlated with the nature of the main crystallising assemblage.

6.2. REE geochemistry

The REE data are displayed in Fig. 5 and Table 4[1]. Relative to unaltered granite compositions, REE are shown to be mobile in the great majority of shear zones (93% of 34 analyses). In most cases, LREE (light REE) are fractionated relative to HREE (heavy REE) (82%), whereas they show no fractionation during alteration in only 18% of cases. The data can be separated into four groups of spectra: (1) REE-depleted without any significant fractionation between LREE and HREE (except for Eu; Fig. 5A), (2) LREE-enriched or less depleted relative to HREE (Fig. 5B), (3) LREE-depleted relative to HREE (Fig. 5C), (4) HREE-enriched relative to LREE (Fig. 5D). There is no relation between the shear zone type or major mineral alteration type (chlorite-, epidote-, actino-

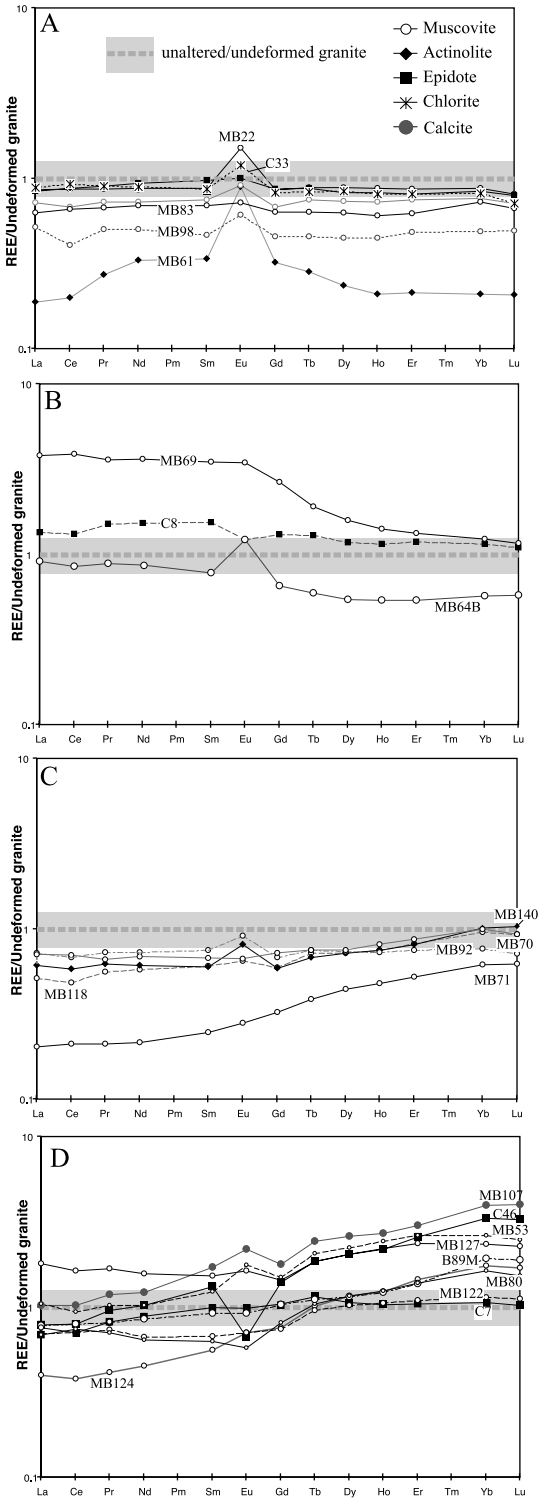

lite-, calcite-bearing or muscovite–biotite–titanite-bearing) and the nature of REE patterns. In contrast, the comparison of REE contents of rocks sampled across a single shear zone (Fig. 6) indicates that there can be coupled gains and losses in REE between shear zones and their immediate environs. For the area in Fig. 6, the damage zone adjacent to the main shear zone is depleted in LREE, whereas the core is selectively enriched in LREE. Depletion in LREE around the main shear zone indicates a preferential LREE leaching process, while LREE enrichments in the core of the shear zone suggest either the precipitation of REE-rich minerals in that area or relative enrichment due to depletion in major elements and consequent volume loss.

6.3. Isocon plots

In order to check if there is a clear decoupling between the REE and the major and other trace element contents, the data for the previously defined four groups of REE patterns are plotted in isocon diagrams (Figs. 7 and 8). Isocon diagrams are used to compare the bulk rock chemistry of rocks that have undergone changes in whole-rock compositions [1,2]. In Figs. 7 and 8, the composition of the shear zone is compared to that of the average undeformed granite. Elements that remain immobile during fluid–rock interaction plot on a line called an isocon, which gives the relation between the shear zone and host rock compositions:

$$C_A = (M_0/M_A)C_0 \quad (1)$$

←

Fig. 5. REE patterns for shear zones. The REE concentrations are normalised to the average REE concentration of Mont Blanc granite. The symbols represent the nature of the main alteration assemblage (muscovite-, chlorite-, epidote-, actinolite-, calcite-bearing). The data can been sorted into four groups of REE-patterns: (A) REE depleted without any significant fractionation between LREE and HREE (except for Eu); (B) LREE enriched or less depleted relative to HREE; (C) LREE depleted relative to HREE; (D) HREE enriched relative to LREE. The shaded area corresponds to the 2σ compositional variation in initial granite host compositions. Note that there is no correlation between the main mineral assemblage type and the REE distribution.

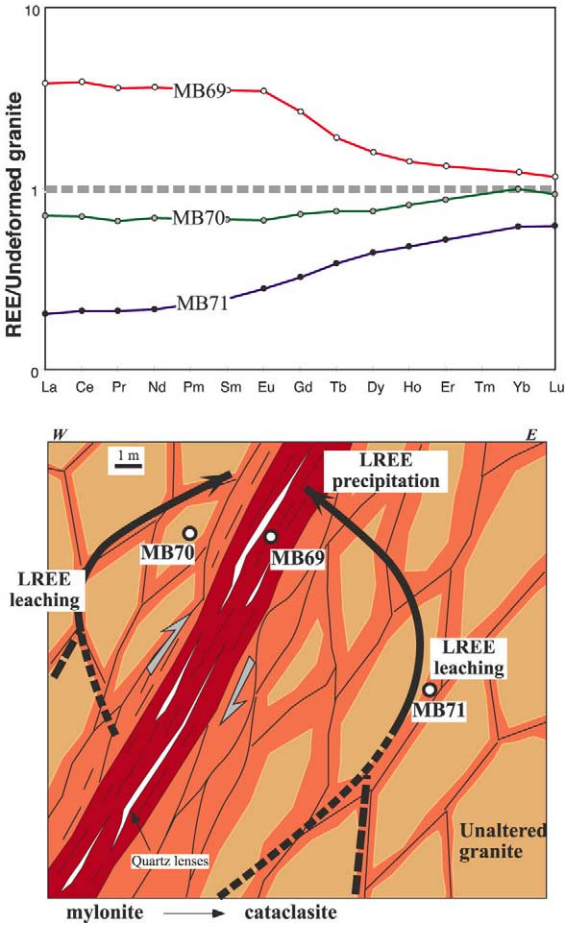

Fig. 6. Sketch to explain the pattern of REE spectra for a shear zone section in the Talèfre area. Note the strong LREE enrichment pattern of the main shear zone core (sample MB69) and the intermediate (MB70) to strong (MB71) LREE depletion patterns of samples from the main shear zone rims. LREE enrichment of the shear zone core is interpreted to result from preferential leaching of LREE at the shear zone rims.

where C_0 and C_A are the element concentrations of the unaltered and the altered granite, respectively. M_0 is the mass of undeformed granite and M_A is that of the altered granite. The ratio M_0/M_A is a function of both enrichment/depletion and of volume change during deformation. Element concentrations plotting above the isocon line indicate enrichment in the altered rock, and depletion if they plot below the isocon. If the isocon has a slope of one, immobile elements have maintained a constant concentration during fluid–rock interaction, and thus no volume change has occurred. In the following examples (Figs. 7 and 8), aluminium is considered immobile, as is suggested by mass-balance calculation in Section 6.1 and Fig. 4. Al immobility is further confirmed

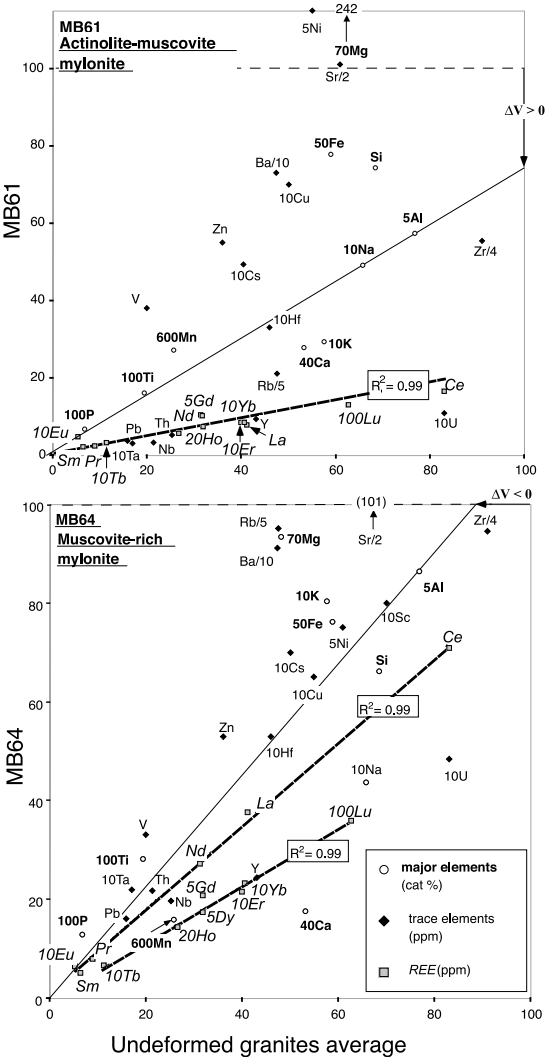

Fig. 7. Isocon plots for two cases of REE depletion. A continuous line indicates the possible isocon line. Diagonal bold discontinuous lines and R^2 values indicate the linear correlations for all the REE in the top diagram or linear correlations for the LREE and HREE, respectively, in the bottom diagram. The nature of the volume change ($\Delta V > 0$ or < 0) is indicated by the bold arrow. The horizontal dashed line indicates the 100 value of the ordinate axis. Units are indicated in the box.

in Figs. 7 and 8 by good linear correlation of Al with Ti and P, which are generally considered immobile by other authors (e.g. [3] and references therein).

In Fig. 7, two representative cases of REE depletion are plotted on isocon diagrams (samples MB61 and MB64). The MB61 diagram features REE depletions without any fractionation of LREE relative to HREE (Fig. 5A). The MB64 diagram (Fig. 7) represents the case of REE depletion with a clear fractionation of LREE relative to HREE (Fig. 5B). In the case of sample MB61, volume gain is shown by depletion in Al and enrichment in Si and inversely for sample MB64. As highlighted in Section 6.1, the behaviour of the mobile major elements is explained by changes in the mineral assemblages. For instance, the marked enrichments in Mg, Fe and Mn in the MB61 plot (Fig. 4) are interpreted to result from the crystallisation of actinolite, while slight depletions in Ca, K and Rb in this plot result from the alteration of plagioclase and K–feldspar. In the case of MB64, enrichments in Mg, relative enrichment or immobility of K, and relative depletion or immobility of Fe are explained by the crystallisation of Mg/Fe-rich biotite and phengite. Strong depletions in Ca are related to the destruction of plagioclase. Enrichment in K is correlated with enrichments in LILE (Rb, Ba, and Sr).

In Fig. 8, various cases of REE enrichment in shear zones have been plotted. The top diagram (MB107) features HREE enrichment and slight LREE enrichment. The bottom two diagrams feature cases of (1) coupled HREE and LREE enrichments (MB127) and (2) strong LREE enrichment with moderate HREE enrichment (MB69). As noticed for the cases of REE depletion illustrated in Fig. 7, the behaviour of REE is again unrelated to the behaviour of major elements (which are controlled by the main mineral assemblage). For instance, MB127 and MB69 have similar metamorphic assemblages (quartz–muscovite), and similar major element enrichments/depletions, but show different REE enrichments.

In cases of both REE depletion or enrichment, linear correlation coefficients on the isocon plots are very high ($R^2 > 0.95$) for both LREE and HREE trends. Some trace elements have a

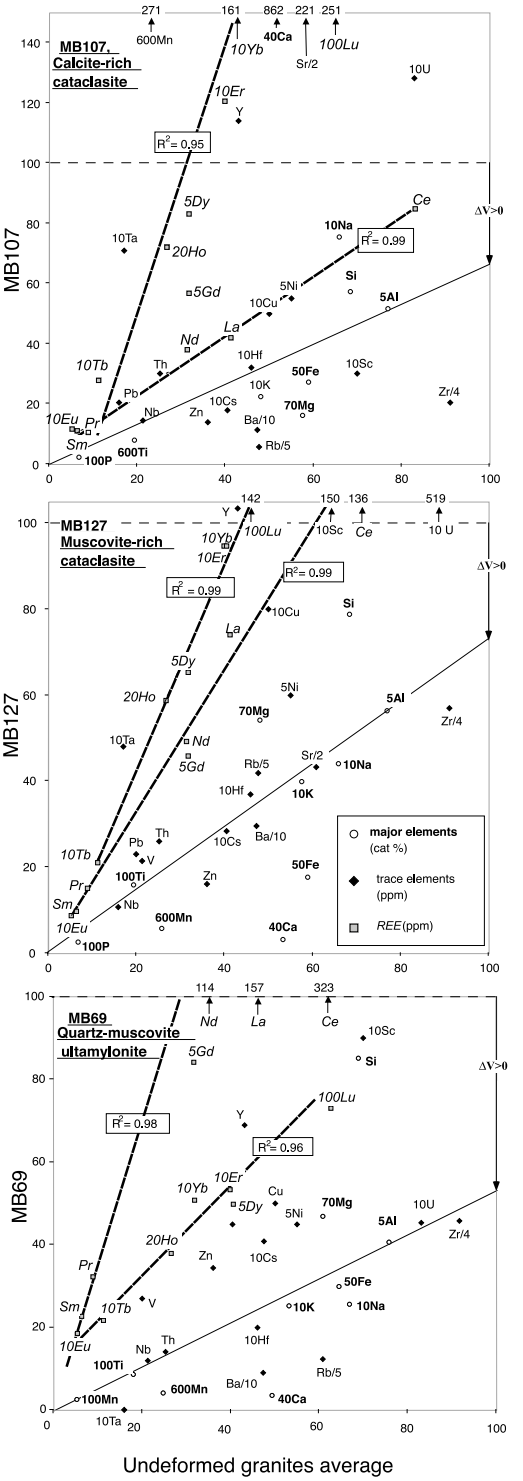

Fig. 8. Isocon plots for various cases of REE enrichments. See Fig. 7 for details of the plots.

behaviour similar to either LREE or HREE. For instance, Y and Ta are fractionated in the same way as HREE. Enrichments in Ta are always more important than in Nb, and this partial decoupling in Nb relative to Ta is also reflected by very variable Nb/Ta ratios in the shear zones in general ($2.03 < Nb/Ta < 33.6$; $Nb/Ta_{unaltered\ granite} = 12.6$). Zr is nearly always depleted, although there are some cases of relative immobility (e.g. MB69, MB64). Surprisingly, Hf contents can be enriched while Zr contents are depleted, which is also reflected in the wide range of Zr/Hf ratios in the samples ($12.8 < Zr/Hf < 40.4$; $Zr/Hf_{unaltered\ granite} = 34$).

In conclusion, the depletion in REE was not caused by volume changes due to shearing, because the observed REE trends in these examples are well below or above the isocon correlation lines (Figs. 7 and 8). Depletions or enrichments in REE, and decoupling of LREE versus HREE, appear to be unrelated to the nature of the main crystallising silicate assemblage or to the intensity of strain. In the next section, we illustrate how this difference in behaviour can be related to the stability of particular REE-bearing minerals, which contain most of the REE budget of the shear zone rocks.

7. REE-bearing phases

7.1. Magmatic REE minerals of the host granite

The REE contents of the host granite are mostly hosted by accessory minerals. Petrographic observations ([26,27], this study) indicate the presence of the following accessory minerals: zircon (1–3%), apatite (0.5–2%) and allanite (0.5–1.5%). Representative LA-ICP-MS analyses are plotted in Table 5[1] and Fig. 9, with representative analyses of the major minerals in the granite: feldspar, quartz (analysed REE contents of biotite are below detection limits). In Fig. 9, LREE contents of allanite and HREE contents of zircon are three to five orders of magnitude above those of other analysed granite minerals. Consequently, the whole-rock REE budget is accounted for by the composition and proportion of the accessory minerals (Table 5[1]). Monazite has not been observed in the host granite, and mass-balance calculations based on the percentage of apatite accounts for the whole-rock P_2O_5 content.

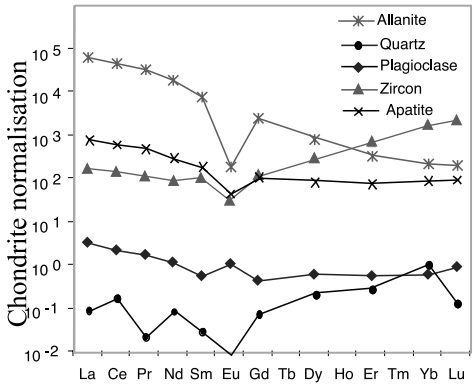

Fig. 9. LA-ICP-MS REE spectra of representative granite host minerals. Note the difference in concentration of REE between REE-bearing and major granite minerals. Plots are normalised to chondritic values of [60].

7.2. Cases of strong LREE enrichment

The quartz–muscovite-bearing mylonite sample MB69 is characterised by very high LREE contents (see Figs. 6 and 8). SEM investigations (Fig. 10A[1]) reveal the presence of mostly < 10 μm grains of REE-rich minerals, mainly bastnäsite [$(Ce,La,Nd)CO_3$]. The bastnäsite grains are found as overgrowths on monazite(-Ce) and allanite crystals. Monazite(-Ce) [$(Ce,La,Nd)PO_4$] and bastnäsite have similar REE compositions (Table 6[1]). LREE contents are very high, namely 23–30 wt% for CeO_2, 13–16 wt% for La_2O_3 and 7–10 wt% for Nd_2O_3. LA-ICP-MS traverses of a large (250 μm) grain show an increase of HREE and a decrease in LREE from core to rim (Fig. 11).

7.3. Cases of strong HREE enrichment

The calcite-bearing cataclasite sample MB107 is selected for its very high HREE and Ta contents (see Figs. 5 and 8). SEM investigations show that small (< 20 μm) and zoned REE-bearing phases of the aeschynite [$(Y,REE,U,Th)(Ti,Nb,Ta,W)_2O_6$] type are formed at the rim of pyrite grains coated by magnetite and within the calcite-rich

matrix of the cataclasite (Fig. 10B[1]). The zonings are correlated with variations in Ti, Y, Nb and Ta (TiO_2: 23–37 wt%, Y_2O_3 = 17–26 wt%, Nb_2O_5: 9–23 wt% and Ta_2O_5: 0–13 wt%; Table 6[1]). The lighter parts of the grains in Fig. 10B[1] are (Nb,Ta)-rich and (Ti,Y)-poor. EPMA analyses show that Nb and Ta are anti-correlated with Ti contents, which suggests Nb,Ta ↔ Ti substitution. These measured mineral compositions fit in with the elemental substitutions in aeschynite proposed by [45,46].

7.4. Cases of LREE and HREE enrichments

The sample MB127 is selected for its generally elevated REE content (see Figs. 5 and 8). EPMA and LA-ICP-MS investigations show the presence of two REE-bearing phases (< 20 μm grains in aggregates) formed within extensional microcracks between feldspar clasts or within the foliated mylonite matrix (Figs. 10C[1] and 11; Table 5[1]):

1. Monazite(-Ce) [(Ce,La,Nd)PO_4]. Analysed monazite grains contain major amounts of Ce (CeO_2: 34–38 wt%), La (La_2O_3: 17–21 wt%), and Nd (Nd_2O_3: 8–10 wt%).
2. Tombarthite [$Y_4(Si,H_4)_4O_{12-x}(OH)_{4+2x}$] (e.g. [47,48]). Analysed tombarthite contains major amounts of Si (SiO_2: 25–32 wt%), Y (Y_2O_3: 21–23 wt%) and HREE (Dy_2O_3: 3.2–4.9 w% and Yb_2O_3: 1.0–1.5 wt%), with minor LREE contents ($La_2O_3 < 1\%$; $CeO_2 < 5\%$). The high concentrations of mid- and H-REE found in this mineral can be explained by substitutions with Y in the mineral lattice.

These two phases have precipitated successively during deformation. Monazite crystallises during a first stage of crack opening while tombarthite fills the core of the crack (Fig. 10C,D[1]) and is interpreted to have formed mainly in a second stage.

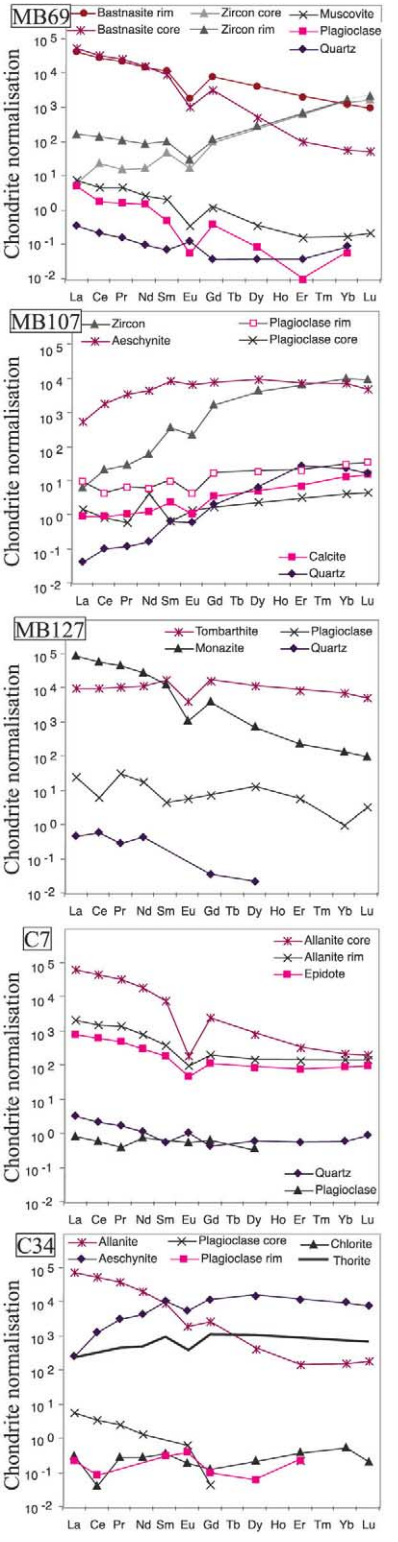

Fig. 11. Single mineral REE spectra obtained by LA-ICP-MS for the most representative shear zone assemblages. Note the difference in concentration of REE between REE-bearing other minerals. Plots are normalised to chondritic values of [60].

7.5. Cases of REE fractionation due to a leaching process

Allanite [$(Ce,La,Ca,Y)_2(Al,Fe)_3(SiO_4)_3(OH)$] is the main repository of REE in the granite host (see Section 7.1). The removal of REE during alteration is illustrated for the case of sample C7, where allanite breaks down into epidote (Fig. 10E,F[1]). The LA-ICP-MS profile obtained on a single allanite crystal (Fig. 11) shows an abrupt decrease of LREE and a conservation of HREE contents from core to rim, the rim being of a composition relatively similar to the average epidote value. The allanite breakdown into epidote is thus responsible for a relative LREE depletion in the shear zone.

Zircon is the most important repository of HREE in the granite host (see Section 7.1). Changes in abundance of REE, Zr and Hf in zircon are illustrated for a single-grain LA-ICP-MS traverse from the mylonite sample MB69 (Fig. 11). HREE contents remain stable from core to rim, while LREE contents increase dramatically ($La_{core} = 1.6$ ppm; $La_{rim} = 38$ ppm; Table 6[1]). The Hf contents increase with respect to Zr, as shown by the decrease of the Zr/Hf ratio from 36 to 24. It is still uncertain if this zoning can be interpreted as an alteration zoning pattern. However, the increase in Zr/Hf ratios in zircon rims of shear zone rocks coincides with an increase in Zr/Hf ratios of whole-rock data, as a result of Zr depletion (Zr being below the isocon line in most cases). Despite the probable influence of alteration on the Zr and Hf contents of the rock, it has only little effect on the whole-rock REE budget, as the variations in LREE in zircon are minor with respect to other phases such as bastnasite.

7.6. Cases of REE re-enrichment after a phase of depletion

In sample C33, previous magmatic REE-bearing minerals have been partly removed during chloritisation but, surprisingly, the final bulk-rock REE contents have not changed significantly relative to the granite protolith (except for Eu) and have not been fractionated. SEM investigations show that the preservation of similar REE contents is not due to the preservation of magmatic allanite. In contrast, textural relationships show that small (<40 μm), newly crystallised REE-rich phases are synchronous with, or have overgrown, the mainly chloritic foliation (Figs. 10[1] and 11). New aeschynite and allanite crystals are euhedral and contain chlorite, uraninite and thorite inclusions. The chemistry of aeschynite reveals two broad compositional varieties that could be distinguished by EPMA (Table 6[1]): (1) a Nb,Y,W-rich, REE-depleted type, with up to 27 wt% Y_2O_3 and 6 wt% Nb, and (2) a REE-rich, Y,Nb,W-depleted type with up to 5 wt% Dy_2O_3, 2.7 wt% Gd_2O_3 and 1 wt% CeO_2. In comparison to the aeschynite observed in HREE-enriched shear zones (sample MB107), the REE–aeschynite variety in C33 is richer in mid-REE, Ti, and W and poorer in HREE, Ta, and Nb (Table 6[1]).

8. Discussion

The behaviour of REE and Y is strongly decoupled from that of other elements (except U, Th, Hf, Ta) in the shear zones. We have shown that this behaviour is unrelated to the style of deformation (cataclasite, mylonite, and ultramylonite), and is largely unrelated to the major mineral alteration assemblage. Furthermore, fractionation of LREE relative to HREE is observed in a majority of cases and again the relative enrichment of either LREE or HREE is unrelated to the kind of deformation and major mineral alteration assemblage. The behaviour of REE can be interpreted as the result of:

A selective leaching process of LREE relative to HREE or HREE relative to LREE, as observed in allanite (and possibly zircon) during hydrothermal alteration associated with shear zone activity.

The stability of fine-grained, trace amounts of REE-bearing minerals (mostly <20 μm), which precipitated from the fluid in the shear zones and contain most of the bulk-rock REE budget.

Every case of fractionation of LREE relative to HREE can be related to the preferential dissolution or growth of two groups of LREE- or HREE-rich phases, namely: monazite, bastnäsite

and allanite for LREE, and aeschynite, tombarthite and zircon for HREE. The REE content in these minerals is between 10^2 and 10^5 times those measured in the main mineral phases (Figs. 9 and 11). The predominance of one or the other species of REE minerals leads to preferential whole-rock enrichments in HREE or LREE. For instance, mass-balance calculations performed using the percentage of minerals (determined using the whole-rock major element data and EPMA mineral analyses) and their REE composition obtained by LA-ICP-MS shows that whole-rock REE enrichments (of up to 5:1, e.g. Tables 1 and 4[1]) are accounted for by the presence of less than 2% of REE-rich minerals in the rocks (Tables 7 and 8[1]), as already shown by [49] for other undeformed granites. Consequently the mobility/immobility of REE in shear zones must be related to the stability and relative abundance of these REE-bearing phases, which is interpreted to be a function of the fluid composition and *PT* conditions. As the shear zones have formed at relatively similar *PT* conditions, it is likely that the stability of the REE minerals is controlled by the fluid, i.e. the pH, oxygen fugacity (fO_2) and the concentrations of potential REE ligands (SO_4^{2-}, CO_3^{2-}, OH^-, F^-, PO_4^{2-}). These REE ligands may precipitate into REE minerals in response to changes in fluid composition, due to fractional crystallisation, fluid–rock reaction, or fluid mixing processes. Precipitation and dissolution of various REE minerals at different stages of shear zone evolution indicate that changes in fluid chemistry occurred during the evolution in the individual shear zones.

In the following discussion, we (1) examine the present understanding of REE behaviour in hydrothermal fluids, and (2) attempt to interpret the selective LREE enrichments or HREE enrichments observed in the Mont Blanc Massif as a function of evolving fluid compositions.

8.1. Controls on the mobility and fractionation of REE in hydrothermal environments

The use of REE contents and isotopes from the REE series in rocks as indicators of geodynamic settings and as geochronometers relies largely upon the fact that these elements have been proven immobile in a large number of contexts [50,51]. However, Wendlandt and Harrison [52] have also shown that REE can be strongly mobilised by carbonic fluids, with a preferential fractionation of LREE versus HREE. As noted by [22], the formation of carbonate complexes is inhibited by low pH, but could control the mobility of REE at higher pH. There is evidence for the mobility of REE in various hydrothermal environments as shown by (1) the chemistry of geothermal waters and (2) the study of altered rocks and REE deposits.

1. REE solubility in hydrothermal systems is generally believed to be dominated by carbonate and fluoride complexes (see review by [22,53]). Elevated concentrations of REE have been described for instance in the Yellowstone hydrothermal waters (at pH 2–4 [54]). These elevated concentrations are interpreted to reflect the availability of complexing agents, mainly SO_4^{2-} for LREE and F^- for HREE (CO_3^{2-} was below detection limit). The work of [55], based on analyses of groundwater samples related to hydrothermal systems, has shown that F^- is also complexed with Al^{3+}, for waters of pH 3.3–5.2, which can inhibit its influence on REE mobility. In other acid groundwater systems, LREE mostly dominate over HREE, REE concentration showing a negative correlation with pH. In near-neutral groundwater systems ($7 < pH < 9$), flat to HREE-enriched patterns are interpreted to result from the predominance of bicarbonate complexes REE–HCO_3, which form preferentially with HREE, while carbonate complexes ($REE(CO_3)^+$) form preferentially with LREE (see [55] and references therein).
2. Studies of altered rocks have shown the presence of LREE/HREE fractionation during fluid–rock interaction and its effects on Sm–Nd and U–Th–Pb radiometric systems [17,56]. Recent work [57] done on the large REE–Nb Bayan Obo Deposit in China has linked the precipitation of LREE-bearing minerals (monazite, bastnäsite, parisite) with fluid chemistries dominated by H_2O, CO_2 (or CO_3^{2-}) and HF. As indicated by fluid inclusion data, high-

XCO_2 fluids (0.2–0.8) are associated with marked LREE enrichments and high La/Nd bastnäsite (La/Nd ~4–5), whereas less marked LREE enrichments are associated with CO_2 contents below detection limits, and low La/Nd (0.6–2) bastnäsite.

8.2. Controls on the mobility and fractionation of REE in the Mont Blanc shear zones

What are the possible ligands for REE in the shear zones, and could they explain the various cases of REE enrichment/depletion that are observed? The elements dissolved in the fluid are reflected in the composition of the fluid inclusions and the minerals precipitated in the veins and shear zones. Fluid inclusions analysed in the Mont Blanc Massif by [36,37,58] have elevated Cl (1 mol%) and Na, K, Ca (each ~0.1 mol%) contents. In general, CO_2 contents are below detection limits, but CO_2-rich fluid inclusions have been analysed in several places by [36]. The crystallisation of calcite in the veins, together with the presence of graphite interlayered with biotite in the shear zones, requires the presence of carbonate complexes or other forms of C in the fluid. Further, the precipitation of pyrite and galena in the veins and shear zones clearly indicates the presence of sulphur complexes in the fluid in at least some shear zones. Finally, the precipitation of fluorite in some veins also shows the presence of fluoride complexes in the fluids. The crystallisation of monazite in some REE-rich samples also indicates the presence of phosphate complexes in fluids migrating through the shear network. Consequently, the minerals precipitated from the fluid show that chloride, sulphur, carbonate, fluoride and phosphate complexes were present.

Which of these complexes could explain the preferential LREE enrichment in the shear zones? The transition from monazite (REE)–PO_4 to bastnäsite (REE)–CO_3 during fluid–rock interaction, observed for the LREE-rich shear zone of the Talèfre area (Section 7.2), suggests a two-stage fluid evolution involving (1) initial precipitation of monazite followed by (2) bastnäsite. This transition implies elevated initial aPO_4^{2-} to form monazite, followed by increase of XCO_2 in the percolating fluid. Similar varieties of bastnäsite with low La/Nd ratios (0.6–1.0) have been analysed by [57] in the Bayan Obo deposit, and were related to measurable CO_2 contents in the fluid inclusions. However, LREE enrichment might not be due to the presence of CO_2 alone. In the LREE-rich shear zone of Fig. 6, the crystallisation of bastnäsite is correlated with that of pyrite, which shows that sulphur complexes were present in the fluid. It is possible that sulphate complexes explain part of the LREE enrichment because SO_4^{2-} preferentially forms complexes with LREE [54]. However, it seems unlikely that chloride complexes were responsible for LREE enrichment, because they are shown to not fractionate the REE [53]. Furthermore, OH^- and F^{4+} form complexes preferentially with HREE [53]. In conclusion, it seems that for the case of the Mont Blanc Massif, LREE enrichment is best explained by the circulation of (1) a PO_4^{2-}-bearing fluid followed by (2) a SO_4^{2-}–CO_2-bearing fluid.

What is the reason for preferential HREE enrichments, and how can we explain the transition from LREE-rich to HREE-rich shear zones?

Textural relationships in LREE–HREE-rich samples (e.g. MB127), indicate a progressive evolution from early preciptation of LREE-rich phases to late precipitation of HREE-rich phases. Several studies dealing with hydrothermal environments explain evolutions from LREE- to HREE-rich fluids by a large difference in solubility of LREE relative to HREE between different types of hydrothermal fluids (e.g. [59]) or by a decrease in temperature, HREE being more soluble at lower temperatures [22,53]. In the case of the Mont Blanc Massif shear zones, no major change of temperature is indicated by mineral parageneses, but the evolution from a LREE enrichment to a HREE enrichment could be due to an evolution of REE solubility associated with a change in the concentration of main ligands in the fluid. OH^-, $(CO_3)^{2-}$, F^{4+} lanthanide complexes are predicted to increase in ionic strength with increasing atomic number in the REE series [53].

If so, the pH value would have a considerable effect on the solubility of HREE. In HREE-enriched shear zones such as MB107 and MB127, pyrite has been transformed into magnetite prior

to the precipitation of HREE-bearing phases (see Section 7.3 and Fig. 10B[1]). The transformation of pyrite into magnetite indicates a change in the fluid composition, from high sulphur fugacity and low pH values (log $fS_2 > -8$ and log $fO_2 < 7$, respectively) to low sulphur fugacity and high pH values (log $fS_2 < -10$ and log $fO_2 > 7$, respectively), the fO_2 being fixed by the graphite–CO_2 buffer [60]. Following the conclusions of Haas [53], the preferential complexing of HREE could well be explained by the increase of $a(OH)^-$ due to increasing pH. This pH increase may result mainly from metamorphic reactions, such as those producing muscovite (e.g. [5]). Consequently, the variability of REE concentrations could be explained by a single-stage shearing event with progressive breakdown of the former granitoid assemblage into the new phyllitic shear zone assemblage.

9. Conclusion

Networks of granite-hosted shear zones in the Mont Blanc Massif have localised fluid flow and fluid–rock reaction during Alpine deformation. During progressive fluid–rock reaction, REE are amongst the most mobile elements analysed, along with Hf and Ta, and major fractionations of LREE relative to HREE have been observed. Changes in REE concentrations are decoupled from changes in major mineral assemblages and related major element changes during fluid–rock interaction in the shear zones. The mobility of REE in shear zones is interpreted to be related to the stability of the REE-bearing minerals and thus directly to the composition of the fluid, since the *PT* conditions of shear zone formation remained within a narrow range. REE depletions are related to the alteration of previous REE-bearing minerals (mainly allanite), whereas REE enrichments are associated with the crystallisation of trace amounts of phases such as monazite, bastnasite, aeschynite and tombarthite, with grain sizes mostly smaller than 20 μm. Widespread fractionation of LREE relative to HREE is explained by the preferential crystallisation of LREE-rich minerals (monazite, bastnäsite, allanite), or HREE-rich minerals (aeschynite, tombarthite). The dissolution and precipitation of such phases explain the variability of REE in shear zones, and the fact that these elements can be either mobile or immobile under the same *PT* conditions and within the same geological context. The occurrence and stability of REE-bearing minerals is interpreted to be controlled by the availability and relative proportions of ligands in the fluid, such as CO_3^{2-}, PO_4^{2-}, SO_4^{2-}, and to the pH. Three successive phases of mineral precipitation and subsequent REE fractionation are distinguished: at low pH (< 7) and high sulphur fugacity values, (1) high PO_4^{2-} contents produce the precipitation of monazite, (2) high CO_3^{2-} contents trigger the precipitation of bastnäsite, both cases producing LREE enrichments. (3) At higher pH (> 7) and lower sulphur fugacity values, the precipitation of OH^-–REE complexes will produce HREE enrichments.

Acknowledgements

The authors wish to thank the staff of the ANU Electron Microscope Unit for their assistance during SEM work, and C. Allen (RSES, ANU) for help during the acquisition of LA-ICP-MS data. This research is supported by the Australian Research Council (ARC) Large Grant. The manuscript greatly benefited from the comments of F. Poitrasson and editorial handling by K. Farley. Further review and comments were provided by G. Franz.*[KF]*

References

[1] R.L. Gresens, Composition-volume relationships of metasomatism, Chem. Geol. 2 (1967) 47–65.
[2] J.A. Grant, The isocon diagram, a simple solution to Gresens' equation for metasomatic alteration, Econ. Geol. 81 (1986) 1976–1982.
[3] D. Marquer, Transferts de matières et déformation des granitoïdes. Aspects méthodologiques, Schweiz. Mineral. Petrogr. Mitt. 69 (1989) 13–33.
[4] J.E. Streit, S.F. Cox, Fluid infiltration and volume-change during mid-crustal mylonitization of Proterozoic granite, King Island, Tasmania, J. Metamorph. Geol. 16 (1998) 197–212.

[5] C.A.J. Wibberley, A.M. McCaig, Quantifying orthoclase and albite muscovitisation sequences in fault zones, Chem. Geol. 165 (2000) 181–196.
[6] A.K. Sinha, D.A. Hewitt, J.D. Rimstidt, Fluid interaction and element mobility in the development of ultramylonites, Geology 14 (1986) 883–886.
[7] T.S. Brewer, B.P. Atkin, Elemental mobilities produced by low-grade metamorphic events. A case study from the Proterozoic supracrustals of southern Norway, Precambr. Res. 45 (1989) 143–158.
[8] K. O'Hara, W.H. Blackburn, Volume-loss model for trace-element enrichments in mylonites, Geology 17 (1989) 524–527.
[9] A.F. Glazner, J.M. Bartley, Volume loss, fluid flow and state of strain in the extensional mylonites from the central Mojave Desert, California, J. Struct. Geol. 5 (1991) 587–594.
[10] O. Vidal, L. Durin, Aluminium mass transfer and diffusion in water at 400-550°C, 2 kbar in the K_2O, Al_2O_3-SiO_2-H_2O system driven by a thermal gradient or by a variation of temperature with time, Mineral. Mag. 63 (1999) 633–647.
[11] K.C. Condie, A.K. Sinha, Rare earth and other trace element mobility during mylonitization: a comparison of the Brevard and Hope Valley shear zones in the Appalachian mountains, USA, J. Metamorph. Geol. 14 (1996) 213–226.
[12] D.M.H. Alderton, J.A. Pearce, P.J. Potts, Rare earth element mobility during granite alteration: evidence from Southwest England, Earth Planet. Sci. Lett. 49 (1980) 149–165.
[13] M. Cathelineau, U-Th-REE mobility during albitization and quartz dissolution of granitoids: evidence from SE French Massif Central, Bull. Mineral. 110 (1987) 249–259.
[14] M. Bau, Rare-earth elements mobility during hydrothermal and metamorphic fluid-rock interaction and the significance of the oxidation state of Europium, Chem. Geol. 93 (1991) 219–230.
[15] M.T. Ménager, C. Menet, J.C. Petit, M. Cathelineau, B. Côme, Dispersion of U, Th and REE by water rock interaction around an intragranite U-vein, Jalerys Mine, Morvan, France, Appl. Geochem. Spec. Issue 1 (1992) 239–252.
[16] Y. Terakado, T. Fujitani, J. Takada, Experimental study on sorption of rare-earth elements and other trace elements during rhyolite-hydrothermal water interactions, Chem. Geol. 106 (1993) 317–330.
[17] Y. Rolland, C. Picard, A. Pêcher, H. Lapierre, D. Bosch, F. Keller, The Cretaceous Ladakh arc of NW Himalaya - slab melting and melt-mantle interaction during fast northward drift of Indian Plate, Chem. Geol. 182 (2002) 139–178.
[18] F. Poitrasson, C. Pin, J.L. Duthou, Hydrothermal remobilization of rare earth elements and its effects on Nd isotopes in rhyolite and granite, Earth Planet. Sci. Lett. 130 (1995) 1–11.
[19] F. Poitrasson, S. Chenery, D.J. Bland, Contrasted monazite hydrothermal alteration mechanisms and their geochemical implications, Earth. Planet. Sci. Lett. 145 (1996) 79–96.
[20] R. Kerrich, I. Allison, R.L. Barnett, S. Moss, J. Starkey, Microstructural and chemical transformation accompanying deformation of granite in shear zones at Mieville, Switzerland, with implications for stress corrosion cracking and superplastic flow, Contrib. Mineral. Petrol. 73 (1980) 221–242.
[21] S. Fourcade, D. Marquer, M. Javoy, $^{18}O/^{16}O$ variations and fluid circulation in a deep shear zone: the case of the alpine ultramylonites from the Aar massif (Central Alps, Switzerland), Chem. Geol. 77 (1989) 119–131.
[22] S.A. Wood, The aqueous geochemistry of the rare-earth elements and Yttrium. 2. Theoretical predictions of speciation in hydrothermal solutions to 350°C at saturation water vapor pressure, Chem. Geol. 88 (1990) 99–125.
[23] P. Baggio, Il granito del Monte Bianco e le sue mineralizzazioni uranifere, Studi e ricerche della divisione geomineraria CNRN, Roma 1 (1958) 1–130.
[24] F. Bussy, Pétrogenèse des enclaves microgrenues associées aux granitoïdes calco-alcalins: exemple des massifs varisque du Mont-Blanc (Alpes occidentales) et miocène du Monte Capanne (Ile d'Elbe, Italie), Mem. Géologie (Lausanne) 7 (1990) 309 pp.
[25] B. Bonin, P. Brändlein, F. Bussy, J. Desmons, U. Eggenberger, F. Finger, et al., Late Variscan magmatic evolution of the Alpine basement, in: J.F. von Raumer, F. Neubauer (Eds.), Pre-Mesozoic Geology in the Alps, Springer, Heidelberg, 1993, pp. 171–201.
[26] F. Bussy, J.F. vonRaumer, U-Pb geochronology of Palaeozoic magmatic events in the Mont Blanc crystalline massif, Western Alps, Schweiz. Mineral. Petrogr. Mitt. 74 (1994) 514–515.
[27] Marro, C., Les granitoïdes du Mont-Blanc en Suisse, Thèse, Fribourg University, 1986, 145 pp.
[28] G. Bertini, M. Marcucci, R. Nevini, P. Passerini, G. Sguazzoni, Patterns of faulting in the Mont Blanc granite, Tectonophysics 111 (1985) 65–106.
[29] Z. Venera, J. von Raumer, The Alpine overprint in the Mont Blanc massif: mesoscopic and microstructural evidence, 13th Annual Meeting of the Swiss Tectonic Studies Group, Geneva, 1 March 1996, 1996.
[30] J. Belliere, On the age of mylonites within the Mont Blanc massif, Geodin. Acta 2 (1988) 13–16.
[31] P. Antoine, J.L. Pairis, B. Pairis, Quelques observations nouvelles sur la structure de la couverture sédimentaire interne du massif du Mont Blanc, entre le Col du Ferret (frontière italo-suisse) et la Tête des Fours (Savoie, France), Géol. Alp. 51 (1975) 5–23.
[32] A. Guermani, G. Pennacchioni, Brittle precursors of plastic deformation in a granite: an example from the Mont Blanc massif (western Alps), J. Struct. Geol. 20 (1998) 135–148.
[33] D. Marshall, H.R. Pfeifer, J.C. Hunziker, D. Kirschner, A pressure-temperature-time path for the NE Mont-Blanc

massif: fluid-inclusion, isotopic and thermobarometric evidence, Eur. J. Mineral. 10 (1998) 1227–12240.
[34] P. Baggio, G. Ferrara, R. Maladora, Results of some Rb/Sr age determinations of the rocks of the Mont Blanc tunnel, Boll. Soc. Geol. It. 86 (1967) 193–212.
[35] J.F. von Raumer, R.P. Ménot, J. Abrecht, G. Biino, The Pre-Alpine evolution of the external massifs, in: J.F. von Raumer, F. Neubauer (Eds.), Pre-Mesozoic Geology in the Alps, Springer, Heidelberg, 1993, pp. 221–240.
[36] B. Poty, La croissance des cristaux de quartz dans les filons sur l'exemple du filon de la Gardette (Bourg d'Oisans) et des filons du massif du Mont-Blanc, Thèse 3e cycle, Mem. 17, Université de Nancy (France), 1969, 162 pp.
[37] B. Poty, H.A. Stadler, A.M. Weisbrod, Fluid inclusion studies in quartz from fissures of the Western and Central Alps, Schweiz. Mineral. Petrol. Mitt. 54 (1974) 717–752.
[38] F. Leutwein, B. Poty, J. Sonet, J.L. Zimmerman, Age des cavités à cristaux du granite du Mont Blanc, C. R. Acad. Sci. Paris 271 (1970) 156–158.
[39] S.M. Eggins, L.P.J. Kinsley, J.M. Shelley, Deposition and fractionation processes during atmospheric pressure laser sampling for analysis by ICP-MS, Appl. Surface Sci. 127–129 (1998) 278–286.
[40] G. Hoschek, Phase relations of a simplified marly rock system with application to the western Hohe Tauern (Austria), Contrib. Mineral. Petrol. 73 (1980) 53–68.
[41] H.J. Massone, W. Schreyer, Phengite geobarometry based on the limiting assemblage with K-feldspar, phlogopite and quartz, Contrib. Mineral. Petrol. 96 (1987) 212–224.
[42] O. Vidal, T. Parra, Exhumation paths of high pressure metapelites obtained from local equilibria for chlorite-phengite assemblages, Geol. J. 35 (2000) 139–161.
[43] O. Vidal, T. Parra, F. Trotet, A thermodynamic model for Fe-Mg aluminous chlorite using data from phase equilibrium experiments and natural pelitic assemblages in the 100-600°C, 1-25 kbar P-T range, Am. J. Sci. 301 (2001) 557–592.
[44] T. Parra, O. Vidal, P. Agard, A thermodynamic model for Fe-Mg dioctahedral K white micas using data from phase-equilibrium experiments and natural pelitic assemblages, Contrib. Mineral. Petrol. 143 (2002) 706–732.
[45] P. Bonazzi, S. Menchetti, Crystal chemistry of aeschynite-(Y) from the Western Alps: residual electron density on difference-Fourier map, Eur. J. Mineral. 11 (1999) 1043–1049.
[46] C. Aurisicchio, C. DeVito, V. Ferrini, P. Orlandi, Nb-Ta oxide minerals from miarolitic pegmatites of the Baveno pink granite, NW Italy, Mineral. Mag. 65 (2001) 509–522.
[47] H. Neumann, B. Nilssen, Tombarthite, a new mineral from Hogetveit, Evje, South Norway, Lithos 1 (1968) 113–123.
[48] M. Fleischer, New mineral names, Am. Mineral. 54 (1969) 327–328.
[49] C.D. Ward, J.M. McArthur, J.N. Walsh, Rare earth elements behaviour during evolution and alteration of the Dartmoor granite, SW England, J. Petrol. 33 (1992) 785–815.
[50] B.L. Cousens, F.J. Spera, P.F. Dobson, Post-eruptive alteration of silicic ignimbrites and lavas, Gran Canaria, Canary Islands: Strontium, neodymium, lead and oxygen isotopic evidence, Geochim. Cosmochim. Acta 57 (1993) 631–640.
[51] S. Barth, F. Oberli, M. Meier, P. Blattner, G.M. Bargossi, G. DiBattistini, The evolution of a calc-alkaline basic to silicic magma system: geochemical and Rb-Sr, Sm-Nd, and $^{18}O/^{16}O$ isotopic evidence from the Late Hercynian Atesina-Cima d'Asta volcano-plutonic complex, Northern Italy, Geochim. Cosmochim. Acta 57 (1993) 4285–4300.
[52] R.F. Wendlandt, W.J. Harrison, Rare earth partitioning between immiscible carbonate and silicate liquids and CO_2 vapour: results and implications for the formation of light rare-earth-enriched rocks, Contrib. Mineral. Petrol. 69 (1979) 409–419.
[53] J.R. Haas, E.L. Shock, D.C. Sassani, Rare earth elements in hydrothermal systems: estimates of standard partial molal thermodynamic properties of aqueous complexes of the rare earth elements at high pressures and temperatures, Geochim. Cosmochim. Acta 59 (1995) 4329–4350.
[54] A.J. Lewis, M.R. Palmer, A.J. Kemp, N.C. Sturchio, The rare earth element geochemistry of acid-sulphate and acid-sulphate-chloride geothermal systems from Yellowstone notional park, Geochim. Cosmochim. Acta 61 (1997) 695–706.
[55] M.J. Gimeno-Serrano, L.F.A. Sanz, D.K. Nordstrom, REE speciation in low-temperature acidic waters and the competitive effects of aluminium, Chem. Geol. 165 (2000) 167–180.
[56] F. Poitrasson, S. Chenery, T.S. Shepherd, Electron microprobe and LA-ICP-MS study of monazite hydrothermal alteration: Implications for U-Th-Pb geochronology and nuclear ceramics, Geochim. Cosmochim. Acta 64 (2000) 3283–3297.
[57] M.P. Smith, P. Henderson, L.S. Campbell, Fractionation of the REE during hydrothermal processes: constraints from the Bayan Obo Fe-REE-Nb deposit, Inner Mongolia, China, Geochim. Cosmochim. Acta 64 (2000) 3141–3160.
[58] C. Fabre, M.C. Boiron, J. Dubessy, M. Cathelineau, D.A. Banks, Palaeofluid chemistry of a single fluid event: a bulk and in-situ multi-technique analysis (LIBS, Raman Spectroscopy) of an Alpine fluid (Mont-Blanc), Chem. Geol. 182 (2002) 249–264.
[59] A.V. Walter, R. Flicoteaux, C. Parron, M. Loubet, D. Nahon, Rare-earth elements and isotopes (Sr, Nd, O, C) in minerals from the Juquia carbonatite (Brazil): tracers of multistage evolution, Chem. Geol. 120 (1995) 27–44.
[60] C.H. Lee, H.K. Lee, S.J. Kim, Geochemistry and mineralization age of magnesian skarn-type iron deposits in the Janggun mine, Republic of Korea, Mineral. Depos. 33 (1998) 379–390.